A Numerical Study on Oscillatory Flow-Induced Sediment Motion over Vortex Ripples

XIN CHEN AND XIPING YU

State Key Laboratory of Hydroscience and Engineering, Department of Hydraulic Engineering, Tsinghua University, Beijing, China

(Manuscript received 22 February 2014, in final form 1 October 2014)

ABSTRACT

A two-dimensional, two-phase flow model is applied to the study of sediment motion over vortex ripples under oscillatory flow conditions. The Reynolds-averaged continuity equations and momentum equations for both the fluid and sediment phases, which include the drag force, the added mass force, the lift force for interphase coupling, and the standard k–ε turbulence model as well as the Henze–Tchen particle turbulence model for closure, are numerically solved with a finite-volume method. The model is effective over the whole depth from the undisturbed sandy bed to the low concentration region above the ripples. Neither a reference concentration nor a pickup function is required over the ripple bed as in a conventional advection–diffusion model. There is also no need to identify the bed load and the suspended load. The study focuses on the effects of erodible ripples on the intrawave flow and sediment motion over the ripples. The computational results show reasonable agreement with the available laboratory data. It is demonstrated that the formation–ejection process of vortices and the trapping–lifting process of sediment over vortex ripples can be well described by the two-phase flow model. The numerical model can also accurately predict the vertical distribution of the mean sediment concentration.

1. Introduction

Ripples as an amazing type of coastal bedform have been attracting interest of the scientific community for more than a century (Pedocchi and Garcia 2009a). They may be categorized into orbital ripples, anorbital ripples, and suborbital ripples, according to their horizontal scale as compared to the near-bed orbital excursion of water particles caused by wave motion (Greenwood and Davis 1984; Pedocchi and Garcia 2009a). It may also be essential to distinguish between the rolling grain ripples and the vortex ripples following Bagnold (1946). The vortex ripples, with their shapes and dimensions jointly determined by the wave-induced near-bed orbital motion of water and the properties of the bed material (Bagnold 1946; Rousseaux 2006), play a major role in the various near-bed dynamic processes in the coastal waters and have been investigated by many researchers around the world.

The vortex ripples are always accompanied by a periodic formation–ejection process of vortices that then have a trapping–lifting effect on bed material (Zedler and Street 2006). They dominate the wave boundary layer structure as well as the entrainment mechanism of bed material and thus contribute substantially to the wave energy dissipation and the sediment transport rate from an overall point of view. Darwin (1883) and Ayrton (1910) carried out the earliest experiments to demonstrate the close relation between the ripples and vortices formed in between them. Bagnold (1946) tried to predict the ripple geometry from the sediment properties and the hydrodynamic conditions with his experiments involving an oscillating tray covered with sediments in a quiescent water tank. Following the boom of coastal engineering research in the 1950s, a large number of experiments have been done in either oscillatory flow tunnels (Carstens et al. 1969; Mogridge and Kamphuis 1972; Lofquist 1978; Sato et al. 1984; Sato and Horikawa 1986; Ribberink and Al-Salem 1994; O'Donoghue and Clubb 2001; Dumas et al. 2005; O'Donoghue et al. 2006; van der Werf et al. 2007; Pedocchi and Garcia 2009b) or wave flumes (Kennedy and Falcon 1965; Dingier and Inman 1976; Faraci and Foti 2002; Thorne et al. 2002; Williams et al. 2004) to look into the various aspects of the phenomenon, and many empirical formulas have been proposed (Camenen 2009; Pedocchi and Garcia 2009a) to

Corresponding author address: Professor Xiping Yu, State Key Laboratory of Hydroscience and Engineering, Department of Hydraulic Engineering, Tsinghua University, Qinghua Yuan 1, Haidian, Beijing, 100084, China.
E-mail: yuxiping@tsinghua.edu.cn

DOI: 10.1175/JPO-D-14-0031.1

describe the characteristics of ripples and the effects of ripples on either fluid flow or sediment transport.

Numerical study on the flow conditions and the sediment motion around a vortex ripple can be traced to Longuet-Higgins (1981) who adopted the discrete vortex method (DVM) to show the periodic formation–ejection process of vortices around a ripple. Longuet-Higgins's (1981) approach was followed by the studies of Sleath (1982), Blondeaux and Vittori (1990, 1991), Hansen et al. (1994), and Malarkey and Davies (2002). The discrete vortex method is advantageous for a presentational description of the vortex formation–ejection process around a ripple, but struggles to represent the flow when it is highly turbulent. Sato et al. (1986) suggested a finite-difference model on a body-fitted curvilinear grid for wave-induced flow over a vortex ripple based on the so called ψ–Ω (streamfunction and vorticity) formulation of fluid flow and k–ε turbulence modeling. The motion of suspended particles in their study was simulated by means of the Monte Carlo method. Sato et al.'s (1986) approach was followed by the work of Aydin and Shuto (1988), Blondeaux and Vittori (1991), and van der Werf et al. (2008). As computational fluid dynamics (CFD) became popular in the last decades, most of the recent investigations (Tsujimoto et al. 1991; Kim et al. 2000; Sleath 2000; Andersen and Faraci 2003; Li and O'Connor 2007) chose to solve the fluid flow around ripples in the original variables (velocity and pressure), though different authors utilized different methods to deal with the turbulence. The standard CFD approach adopts the Reynolds-averaged Navier–Stokes equations (RANS) as the governing equations of the fluid phase. However, a relatively recent study by Chang and Scotti (2003) showed that large-eddy simulation (LES) might be necessary at least when accurate results on the turbulent behavior of the flow are required. LES in a boundary-fitted curvilinear coordinate system was proposed by Chou and Fringer (2010). It is common in almost all CFD approaches that an additional advection–diffusion equation on the sediment concentration must be solved with the bottom boundary condition given by an empirical formula for the pickup rate or the reference concentration. Such an empirical formula can hardly represent the real physics in general and is usually a source of inaccuracy.

A generally valid numerical simulation of the flow and sediment motion around ripples relies on an effective two-phase flow model that can deal with the hyper-concentrated sediment-laden flow near an erodible bed. Although two-phase flow models have been extensively developed in the recent years (Elghobashi and Abou-Arab 1983; Hsu et al. 2004; Longo 2005; Bakhtyar et al. 2009; Jha and Bombardelli 2009; Chen et al. 2011a,b), an application of such advanced models to the sediment-laden oscillatory flow over ripples has not yet been attempted. The present study is aimed at showing the effectiveness of the model proposed by the authors (Chen et al. 2011b) when applied to the flow and the sediment motion over an erodible ripple bed under wave action. In the following sections, we first give a brief description of the numerical model. Then, we present the numerical results and compare them with available experimental data.

2. Numerical model

a. Basic equations and numerical methods

We use a two-phase flow model of the two-fluid type to describe the sediment-laden flow over vortex ripples. The Reynolds-averaged continuity equations for the sediment phase and the mixture and the Reynolds-averaged equations of motion for both the sediment and the fluid phases are chosen to form the governing equation system following Chen et al. (2011b):

$$\frac{\partial \alpha_f u_{f,j}}{\partial x_j} + \frac{\partial \alpha_s u_{s,j}}{\partial x_j} = 0, \tag{1}$$

$$\frac{\partial \alpha_s}{\partial t} + \frac{\partial \alpha_s u_{s,j}}{\partial x_j} = \frac{\partial}{\partial x_j}\left(\kappa \frac{\partial \alpha_s}{\partial x_j}\right), \tag{2}$$

$$\begin{aligned}\frac{\partial(\alpha_f u_{f,i})}{\partial t} &+ \frac{\partial(\alpha_f u_{f,i} u_{f,j})}{\partial x_j} \\ &= -\frac{\alpha_f}{\rho_f}\frac{\partial p}{\partial x_i} + \frac{\partial}{\partial x_j}\left[\alpha_f(\nu_{f0}+\nu_{ft})\left(\frac{\partial u_{f,i}}{\partial x_j} + \frac{\partial u_{f,j}}{\partial x_i}\right)\right] \\ &\quad + \alpha_f g_i + \frac{\partial}{\partial x_j}\left[\kappa\left(u_{f,i}\frac{\partial \alpha_f}{\partial x_j} + u_{f,j}\frac{\partial \alpha_f}{\partial x_i}\right)\right] - \frac{F_i}{\rho_f},\end{aligned} \tag{3}$$

$$\begin{aligned}\frac{\partial(\alpha_s u_{s,i})}{\partial t} &+ \frac{\partial(\alpha_s u_{s,i} u_{s,j})}{\partial x_j} \\ &= -\frac{\alpha_s}{\rho_s}\frac{\partial p}{\partial x_i} + \frac{\partial}{\partial x_j}\left[\alpha_s(\nu_{s0}+\nu_{st})\left(\frac{\partial u_{s,i}}{\partial x_j} + \frac{\partial u_{s,j}}{\partial x_i}\right)\right] \\ &\quad + \alpha_s g_i + \frac{\partial}{\partial x_j}\left[\kappa\left(u_{s,i}\frac{\partial \alpha_s}{\partial x_j} + u_{s,j}\frac{\partial \alpha_s}{\partial x_i}\right)\right] + \frac{F_i}{\rho_s}, \quad \text{and}\end{aligned} \tag{4}$$

$$\alpha_s + \alpha_f = 1, \tag{5}$$

where α is the volumetric concentration; u is the velocity; p is the pressure; F is the interphase force; the subscripts f and s stand for the fluid and the sediment phase, respectively; the indices i and j are used in accordance with the summation convention; x is the Cartesian coordinate; t is the time; ρ is the density; g is the gravity acceleration; $\kappa = \nu_{ft}/\delta_s$ is the mixing coefficient and δ_s is the Schmidt number; ν_{f0} is the molecular viscosity of the fluid phase; ν_{ft} is the eddy viscosity of the fluid phase; ν_{s0} is the viscosity introduced to model the intergranular stress; and ν_{st} is the turbulent viscosity of the sediment phase. Based on a k–ε turbulence model, the turbulent viscosity of the fluid phase is expressed by $\nu_{ft} = C_\mu k_f^2/\varepsilon_f$, where C_μ is an empirical constant ($C_\mu = 0.09$ in the standard k–ε model for pure water) and k_f and ε_f are the turbulent kinetic energy and the turbulent kinetic energy dissipation rate of the fluid phase. The turbulent viscosity of the sediment phase is expressed by $\nu_{st} = \nu_{ft}(1 + \tau_s/\tau_f)^{-1}$, according to Hinze–Tchen's particle turbulence model (Hinze 1975), where $\tau_f = 1.22C_\mu^{0.75}k_f/\varepsilon_f$ is the turbulence time scale of the fluid phase, $\tau_s = \rho_s D_s^2[18\rho_f\nu_{f0}(1+0.15\mathrm{Re}_s^{0.687})]^{-1}$ is the response time of the sediment, D_s is the sediment particle diameter, and $\mathrm{Re}_s = |\mathbf{u}_f - \mathbf{u}_s|D_s/\nu_{f0}$ is the particle Reynolds number, where the bold face denotes a vector. The viscosity representing the intergranular stress is given by $\nu_{s0} = 1.2\gamma^2\nu_{f0}\rho_f/\rho_s$, according to Ahilan and Sleath (1987), where $\gamma = 1/[(\alpha_{sm}/\alpha_s)^{1/3} - 1]$ and α_{sm} is the maximum sediment volumetric concentration of the undisturbed bed. The terms k_f and ε_f are governed by

$$\frac{\partial(\alpha_f k_f)}{\partial t} + \frac{\partial(\alpha_f k_f u_{fj})}{\partial x_j} = \frac{\partial}{\partial x_j}\left(\alpha_f \nu_{fk}\frac{\partial k_f}{\partial x_i}\right) + \alpha_f(G_f - \varepsilon_f), \quad \text{and} \tag{6}$$

$$\frac{\partial(\alpha_f \varepsilon_f)}{\partial t} + \frac{\partial(\alpha_f \varepsilon_f u_{fj})}{\partial x_j} = \frac{\partial}{\partial x_j}\left(\alpha_f \nu_{f\varepsilon}\frac{\partial \varepsilon_f}{\partial x_i}\right) + \frac{\alpha_f\varepsilon_f}{k_f}(C_1 G_f - C_2\varepsilon_f), \tag{7}$$

where

$$G_f = \nu_{ft}\frac{\partial u_{f,i}}{\partial x_j}\left(\frac{\partial u_{f,i}}{\partial x_j} + \frac{\partial u_{f,j}}{\partial x_i}\right) \tag{8}$$

and $\nu_{fk} = \nu_{ft}/\delta_k$, $\nu_{f\varepsilon} = \nu_{ft}/\delta_\varepsilon$, $\delta_k = 1.0$, $\delta_\varepsilon = 1.3$, $C_1 = 1.44$, and $C_2 = 1.92$. We may have to mention that turbulence production due to the interphase force has been neglected in (6) and (7). The buoyancy production is also neglected, but its effect on the turbulent diffusion is included in an overall modification to the empirical constant C_μ, which is necessary anyhow because the important effect of sediment concentration on the particle turbulence has also been omitted. In the present study, we let $C_\mu = 0.09(1 - \alpha_s/\alpha_{sm})^5$, following Chen et al. (2011a).

The interphase force in (3) and (4) is assumed to include the drag force, inertia force, and lift force, that is,

$$\mathbf{F} = C_D\frac{3\rho_f\alpha_s}{4D_s}|\mathbf{u}_f - \mathbf{u}_s|(\mathbf{u}_f - \mathbf{u}_s) + C_M\rho_f\alpha_s\frac{d(\mathbf{u}_f - \mathbf{u}_s)}{dt} + C_L\rho_f\alpha_s(\mathbf{u}_f - \mathbf{u}_s)\times\mathbf{\Omega}, \tag{9}$$

where $\mathbf{\Omega}$ is the vorticity of the fluid phase, C_D is the drag coefficient given by Schiller and Naumann's (1935) formula but includes the concentration modification factor of Tam (1969), $C_M = 1/2$ is the added mass force coefficient, and $C_L = 1.0$ is the lift force coefficient.

For numerical solutions, (1)–(4) along with (6) and (7) are discretized over a staggered grid by means of the finite-volume method, while the convection and the diffusion terms are treated with the third-order QUICK scheme and the second-order central difference scheme, respectively. Time stepping follows the standard strategy of computational fluid dynamics; that is, the continuity equation for the sediment phase is solved first to obtain the sediment concentration. Then, the momentum equations are used to predict the velocities. Thus, the pressure can be obtained by solving a pressure correction equation derived from the overall mass conservation equation. As a consequence, the velocity components can be corrected to ensure the conservation of momentum more accurately. As long as the volumetric concentration and the velocity of each phase are determined, the discretized equations of (6) and (7) readily yield the values of the turbulence kinetic energy and the turbulence kinetic energy dissipation rate.

The two-phase flow model described above has been shown to be valid for the wave-induced sheet flows (Chen et al. 2011a) and is applicable over the whole depth from the undisturbed sandy bed below the maximum depth of scour to the height where sediment particles can hardly reach. The model is advantageous also because it does not require an identification of the interface between moving and unmoving layers. There is also no need to separate the bed load and the suspended load. Neither a reference concentration nor a pickup function should be prescribed over the ripple bed as is usually necessary in a conventional advection–diffusion model.

b. *Definition of problem*

We focus on the dynamic process of intrawave water and sediment motion over regular sand ripples with known equilibrium profiles. One may expect a description on the deformation process of the ripple as a consequence of the interactions between the flow and

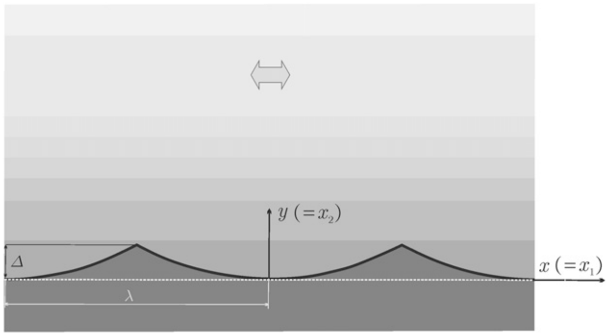

FIG. 1. Definition of problem for oscillatory, flow-induced sediment motion over vortex ripples.

ripple as in Chou and Fringer (2010). That is certainly important if we are interested in the relation between the ripple geometry and flow conditions, in the evolution of the ripple geometry, or in the translation of ripples in the direction of wave motion. However, if we limit our interest to the effects of the ripple on the intrawave flow and sediment motion, the geometry of the ripple rather than its gradual deformation should play the dominant role (Andersen 1999). For this reason and also for consistency with the experimental cases considered in this study, we adopt the physical model shown in Fig. 1. Taking two ripples in the horizontal direction is to assure the spatial repeatability of the numerical results.

Since the ripple development process is omitted, some special considerations become necessary in order to retain the stable profile of the ripple in the numerical computations. In the following study, an originally ripple-shaped bottom is assumed to be undeformable in each case until the flow reaches a periodically stable state. Then, the bottom is allowed to be erodible, but an undisturbed ripple-shaped boundary with volumetric concentration of α_{sm} is intentionally prescribed at a certain distance below the original bottom, where α_{sm}, the maximum concentration corresponding to a loosely packed sandy bed, is taken to be 0.6. The distance between the initial bed and the undisturbed boundary as normalized by the sediment particle size is initially assumed to be 3 times the Shield number estimated over a flat bottom and is eventually determined by trial and error in each computational case to ensure that the undisturbed boundary is indeed undisturbed. The initial and undisturbed ripple profile is related to the flow conditions as suggested by Sleath (1984) and Lewis et al. (1995) and is either represented by

$$y = \Delta\left(1 - 2\frac{|x|}{\lambda}\right)^2; \quad |x| \le \frac{\lambda}{2} \tag{10}$$

or by

$$x = \xi - \frac{\Delta}{2}\sin\frac{2\pi}{\lambda}\xi; \quad y = \frac{\Delta}{2}\left(1 + \cos\frac{2\pi}{\lambda}\xi\right) \tag{11}$$

for sharp-crested and round-crested ripples, respectively, where $x \equiv x_1$ and $y \equiv x_2$ are coordinates; Δ is the height of the ripple, λ is the wavelength of the ripple, and ξ is an auxiliary variable with $\xi = k\lambda$ representing the ripple crest and $\xi = (k + 0.5)\lambda$ representing the ripple trough. Equations (10) and (11) have been well validated. At the undisturbed boundary, the fluid phase should be nearly static. Thus, the velocity components of the two phases as well as the statistical quantities that characterize the turbulence must all be set to zero. The sediment concentration at this boundary is given by $\alpha_s = \alpha_{sm}$. At the moment when the bottom is allowed to be erodible, the flow parameters below the original bed are all set to zero, and the concentration of the sediment is given by $\alpha_s = \alpha_{sm}$ below and $\alpha_s = 0$ above the original bed.

The top boundary of our physical model is at least 5Δ away from the ripple crest such that a "rigid-lid" assumption can be made. The relevant boundary condition thus requires the sediment flux, the gradient of both the

TABLE 1. Representative parameters of cases studied.

Computational cases		T (s)	U_m (m s^{-1})	D_{50} (mm)	Δ (cm)	λ (m)	Ripple shape	Flow condition
Sleath (2000)		4.5	0.114	0.2	1.7	0.10	Smooth	Oscillatory flow
Fredsoe et al. (1999)		2.5	0.255	—	3.5	0.22	Sharp	Wave-induced flow
Nakato et al. (1977)		1.8	0.266	0.14	1.2	0.085	Smooth	Oscillatory flow
Villaret and Perrier (1992)		1.5	0.3	0.09	0.7	0.048	Smooth	Wave-induced flow
Steetzel (1984)	T226	1.0	0.2	0.22	0.5	0.047	Smooth	Oscillatory flow
	T235	1.0	0.3	0.22	0.8	0.053	Smooth	Oscillatory flow
	T260	1.0	0.5	0.22	1.1	0.088	Smooth	Oscillatory flow
	T264	1.0	0.75	0.22	2.0	0.30	Smooth	Oscillatory flow
Williams et al. (1998)		5.0	0.7	0.33	4.8	0.29	Smooth	Wave-induced flow
van der Werf et al. (2007, 2008)		5.0	0.63	0.44	7.8	0.41	Smooth	Oscillatory flow

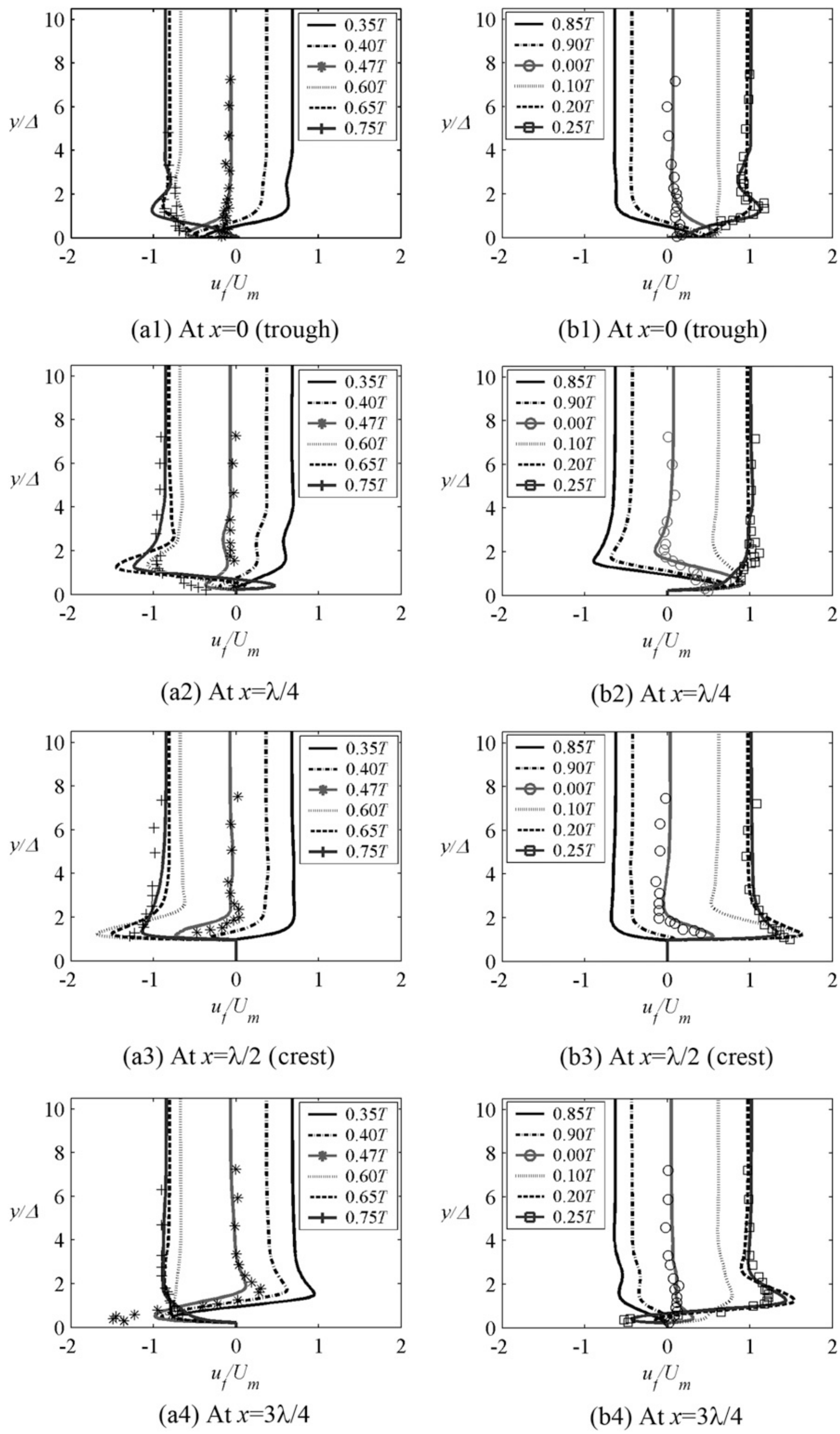

FIG. 2. Comparison of the horizontal velocity at different cross sections over vortex ripples computed by the two-phase flow model with Fredsoe et al.'s (1999) experimental measurements. Variation of the velocity profile within a period is divided into two columns for clarity.

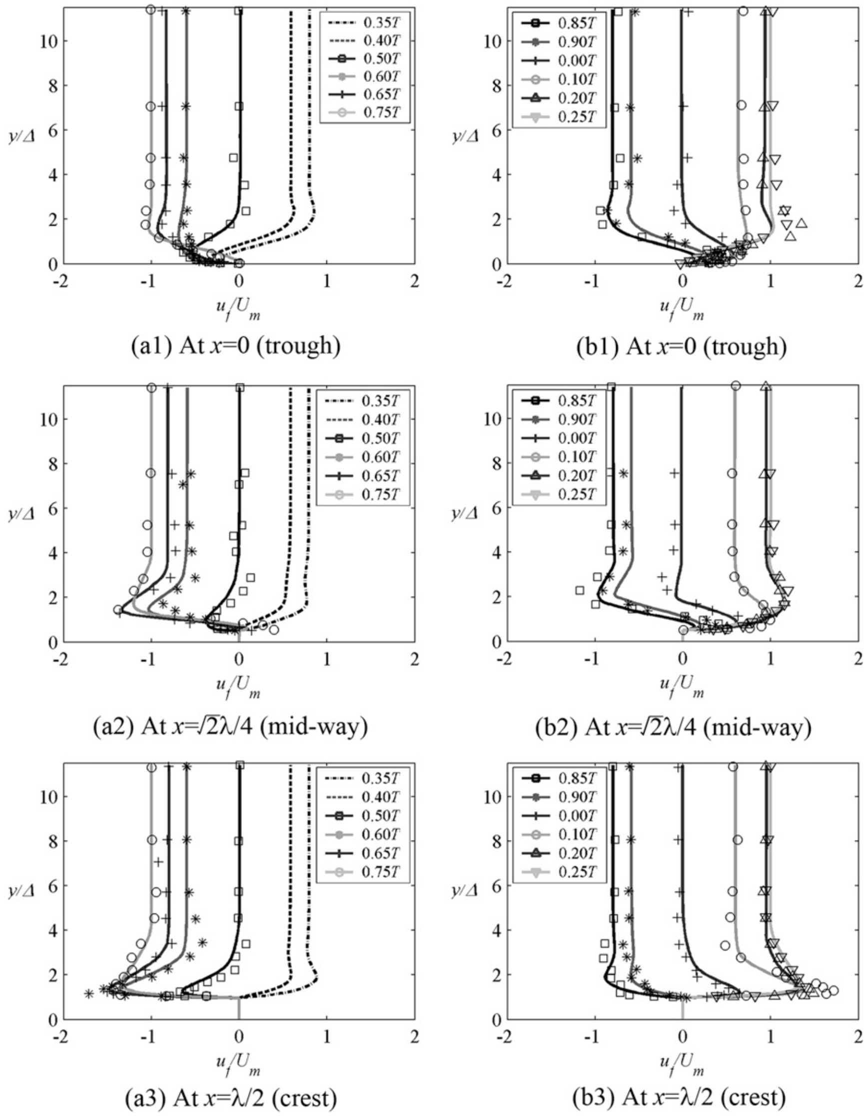

FIG. 3. Comparison of the horizontal velocity at different cross sections over vortex ripples computed by the two-phase flow model with Sleath's (2000) experimental measurements.

horizontal and vertical velocity components of the fluid and the sediment phases, the turbulence kinetic energy, and the turbulence kinetic energy dissipation rate to be zero in the vertical direction. The horizontal velocity of the fluid at the top boundary is given according to the free-stream velocity in an oscillatory flow tunnel. It corresponds to the outer flow velocity of the relevant bottom boundary layer problem if the ripples are generated by a surface wave. "Slip" of the sediment along the top boundary is also allowed. No flux of the sediment in the vertical direction of the top boundary requires that

$$\kappa\frac{\partial\alpha_s}{\partial y} - u_{s,2}\alpha_s = 0. \tag{12}$$

The periodic conditions are given at the lateral boundaries for all variables.

3. Results and discussions

a. Computational conditions

The cases of interest in the present study are carefully selected from a large number of laboratory investigations in the literature on the effects of the vortex ripples under oscillatory flow conditions, including Fredsoe et al.'s (1999) and Sleath's (2000) experiments that focused on the periodic flow of the fluid phase and Nakato et al.'s (1977), Villaret and Perrier's (1992),

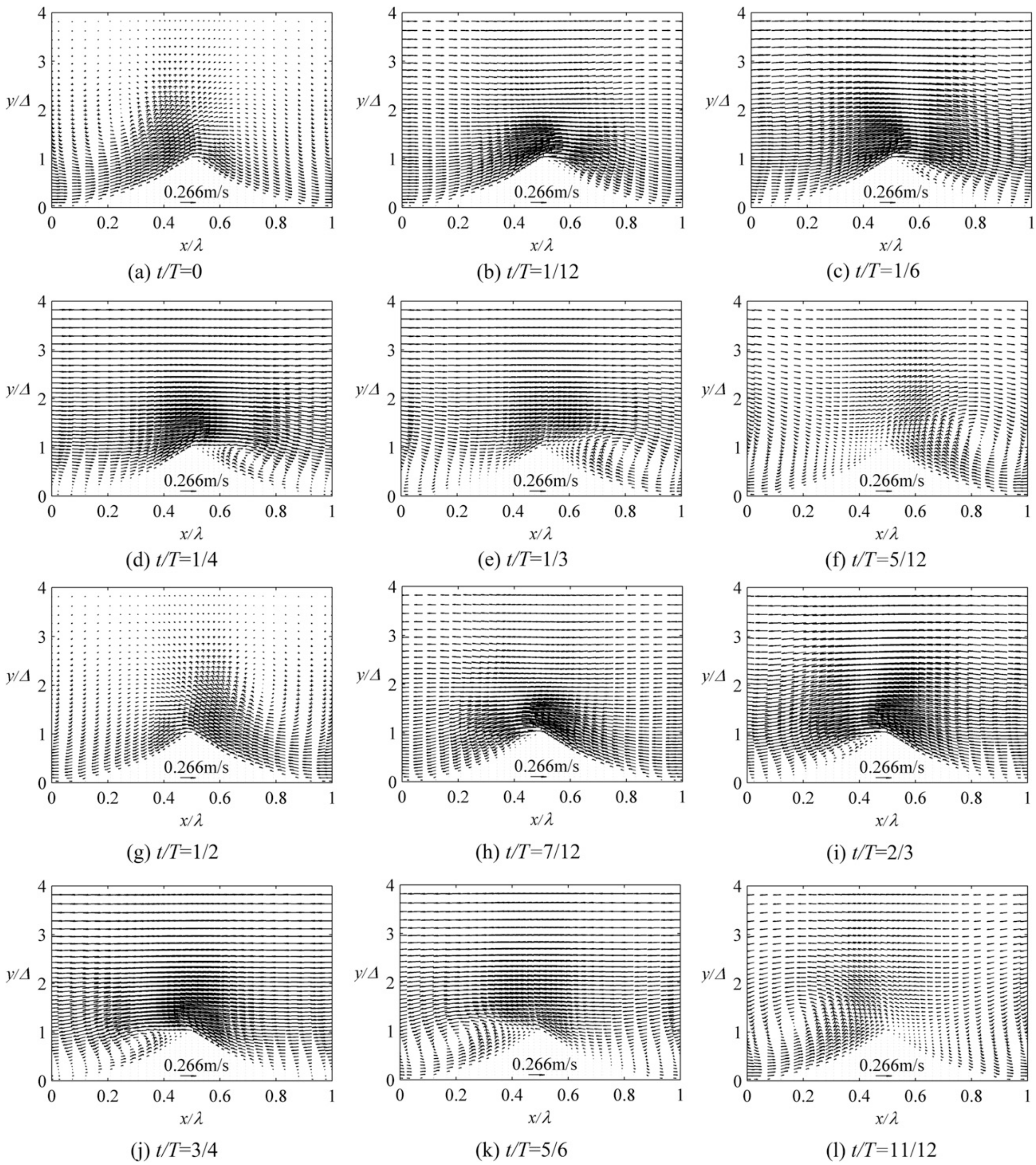

FIG. 4. Computed velocity of Nakato et al.'s (1977) experimental case.

Steetzel's (1984), Williams et al.'s (1998), and van der Werf et al.'s (2007, 2008) experiments that studied the periodic variation of the sediment concentration. Table 1 summarizes the representative parameters of the cases referred to in this study, including the ripples shapes, where T is the wave period, U_m is the maximum free-stream velocity, and D_{50} is the median sediment diameter.

In all the computations, the domain is fixed to two ripple lengths in the horizontal direction and to match the experimental water depth in the vertical direction. We adopt the rectangular grid for convenience. To

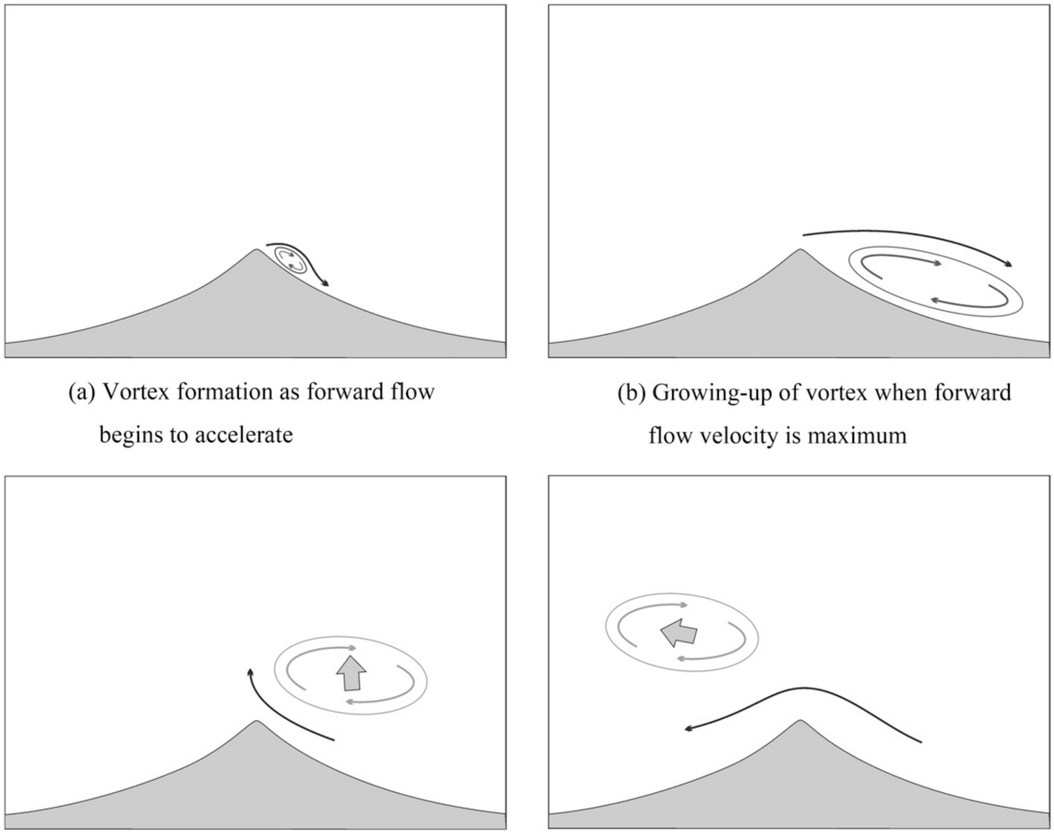

(a) Vortex formation as forward flow begins to accelerate

(b) Growing-up of vortex when forward flow velocity is maximum

(c) Rise of vortex due to decelerated forward flow

(d) Sweeping of vortex due to backward flow

FIG. 5. Sketch of vortex formation–ejection process.

obtain the details of the sediment motion near the bottom with reasonable efforts of computation, a varying grid size is considered; that is, we let the vertical grid size be equivalent to the sediment diameter nearby the bottom and increase linearly in the upward direction. The horizontal grid size is also set to be fine near the ripple crest and increases toward the ripple trough. Eventually, the vertical grid size varies from a minimum of 0.1 mm near the bottom to a maximum of 5.0 mm at the top, and the horizontal grid size varies from a minimum of 0.7 mm over the ripple crest to a maximum of 5.0 mm over the ripple trough. To ensure a steady-state solution, the computation for each case is continued for 10 to 20 wave periods until the relative difference of the concentration and velocity of each phase between two adjacent cycles reached a prescribed level of 10^{-4}. The last cycle of the computation is then taken as the final result. It is found that the relative difference between the corresponding points over the two ripples included in the computational domain is also less than a level of 10^{-4} as long as the prescribed accuracy between the two adjacent cycles is reached. We then take the average of the computational results over the two ripples to represent the fluid and the sediment motion in the present study. The computational time required for a typical case is about 15 to 20 h by a desktop computer with 3.5-GHz CPU.

b. *Flow of fluid phase*

We first consider Fredsoe et al.'s (1999) case, which concerns clear water flow over a solid bed of fixed ripples. The free-stream velocity corresponds to a second-order Stokes wave-induced bottom flow and is given by $U = U_1 \cos\sigma(t + t_0) + U_2 \cos 2\sigma(t + t_0)$, where $U_1 = 0.235\,\mathrm{m\,s^{-1}}$, $U_2 = 0.020\,\mathrm{m\,s^{-1}}$, $\sigma = 2\pi/T$ is the angular frequency, and $t_0/T = 0.0275$. The initial phase is introduced so that $U = 0$ at $t = 0$. The positive direction of the free-stream velocity is related to the onshore direction and negative direction to the offshore direction for real coastal waves. Figure 2 shows the horizontal velocity at the different phases of the flow within a period at several cross sections. The computed results

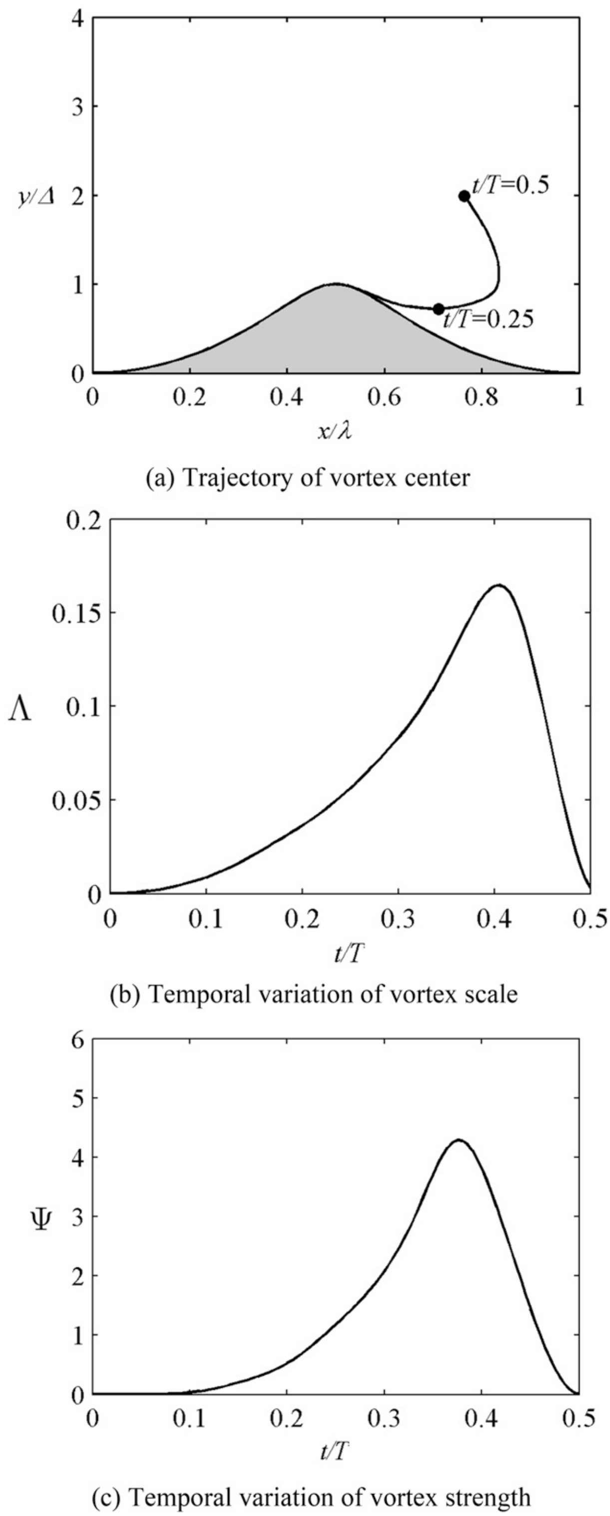

FIG. 6. Trajectory of vortex center and temporal variation of vortex scale and strength.

(lines) are compared with available experimental data (symbols) at $t/T = 0$, 0.25, 0.47, and 0.75. The computation is shown to agree very well with the experiment except for some discrepancies near the bed at some phases when the variation of the flow in the vertical direction is very rapid so that both the experimental and computational results are sensitive to the phase and location. It is also noted that the variation of the horizontal velocity over the ripple crest is rather similar to that in an oscillatory boundary layer (Mellor 2002; Nielsen 1992; Malarkey and Davies 2004) except for a larger velocity overshoot near the bed. In an oscillatory boundary layer, the velocity overshoot in the horizontal velocity profile is thought to be caused by the phase shift within the boundary layer. The velocity overshoot in the present situation is probably also related to the intensification of the local flow caused by the ripple crest constriction. The wavy variation of the horizontal velocity at other vertical cross sections over the ripple, which is of a vertical scale equivalent to the ripple height, is obviously because of the periodically shed vortex that always accompanies the oscillatory flow over a ripple (Nielsen 1992).

To study the oscillatory flow over sandy ripples, we applied our numerical model to the experimental case of Sleath (2000). In this case, the bed is deformable while the free streamflow is sinusoidal. Figure 3 is a comparison of the computed vertical variation of the horizontal velocity over the crest ($x = \lambda/2$), the trough ($x = 0$), and a midway point ($x = \sqrt{2}\lambda/4$) of the ripple with available experimental data at several phases of the free streamflow. The computation (lines) agrees very well with the experiment (symbols). It can also be seen that the symmetry of the flow within a wave period is reasonably preserved by comparing the velocity profiles at $t/T = 0$ and 0.1 with those at $t/T = 0.5$ and 0.6 over the ripple crest and trough, respectively. When compared with the results of Fredsoe et al.'s (1999) case as shown in Fig. 2, it is not difficult to find that the phase shift within the bottom boundary layer over a deformable bed is different from that over a solid bed. In fact, the reverse of the maximum velocity falls much behind the free-stream velocity in Fig. 3, and this is not what showed in Fig. 2. Wavy variations of the horizontal velocity over the midway point and the trough of the ripple still exist, indicating that vortex shedding occurred.

c. Periodic vortex shedding due to ripples

Figure 4 presents the computed flow field within a wave period of Nakato et al.'s (1977) experimental case. A vortex formation–ejection process, as reported to a different extent in the previous studies (Ranasoma and Sleath 1992; Hansen et al. 1994; Malarkey and

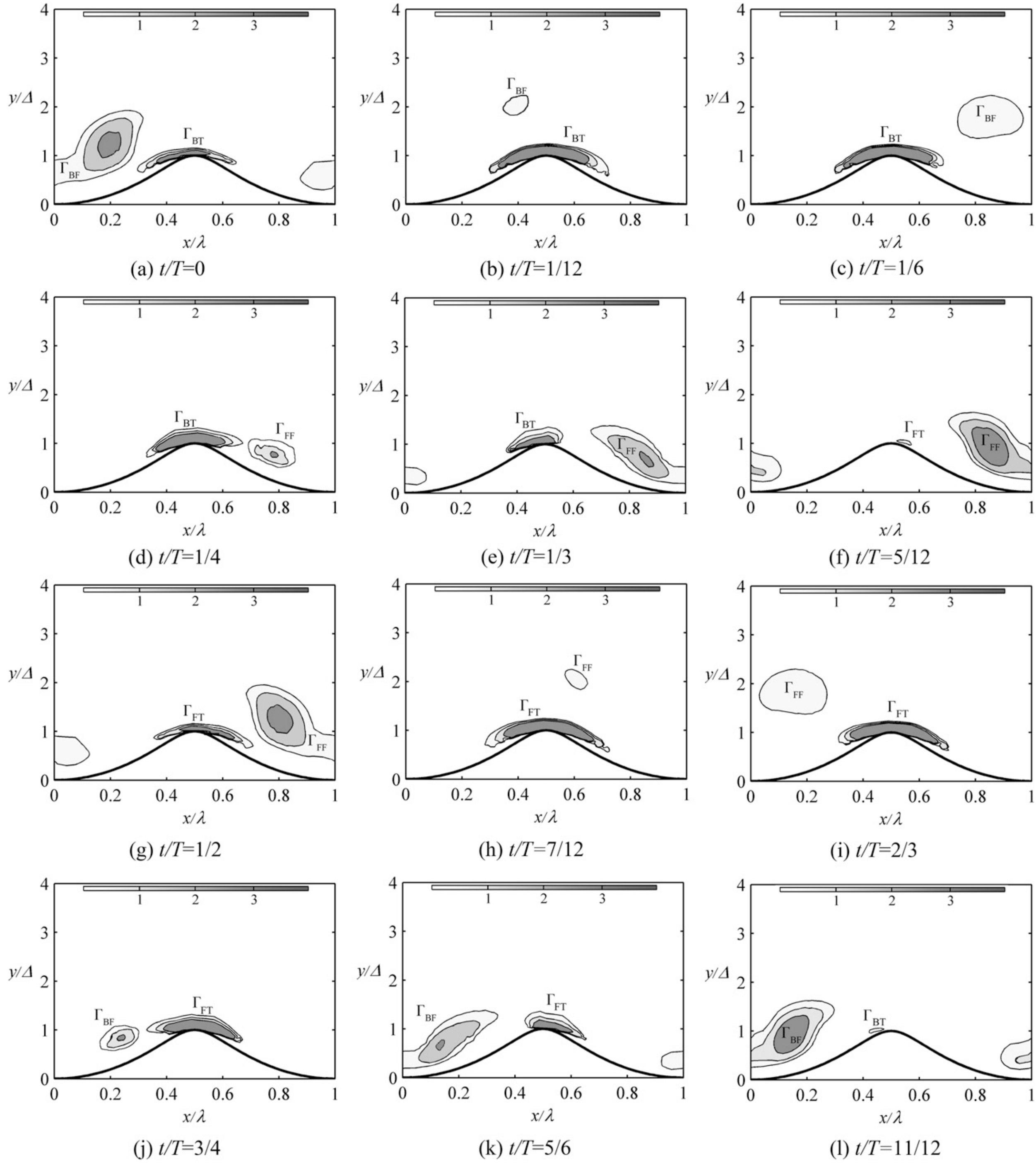

FIG. 7. Computed nondimensional swirling strength $\Phi\lambda/U_m$ of Nakato et al.'s (1977) experimental case.

Davies 2002; Zedler and Street 2006), is clearly shown. Shortly after $t/T = 0$ when the free-stream velocity becomes positive, a clockwise vortex starts to form near the ripple crest next to the right-hand (lee) side below the previous anticlockwise vortex (Fig. 4b). As the free streamflow accelerates, the clockwise vortex grows in both size and strength (Figs. 4b–d). When the free streamflow decelerates, a rise of the vortex can be observed, while a strong reverse flow beneath the vortex develops (Figs. 4e–f). The vortex arises slowly at the beginning, but it is quickly ejected to its highest position after $t/T = 5/12$. As the free streamflow changes its

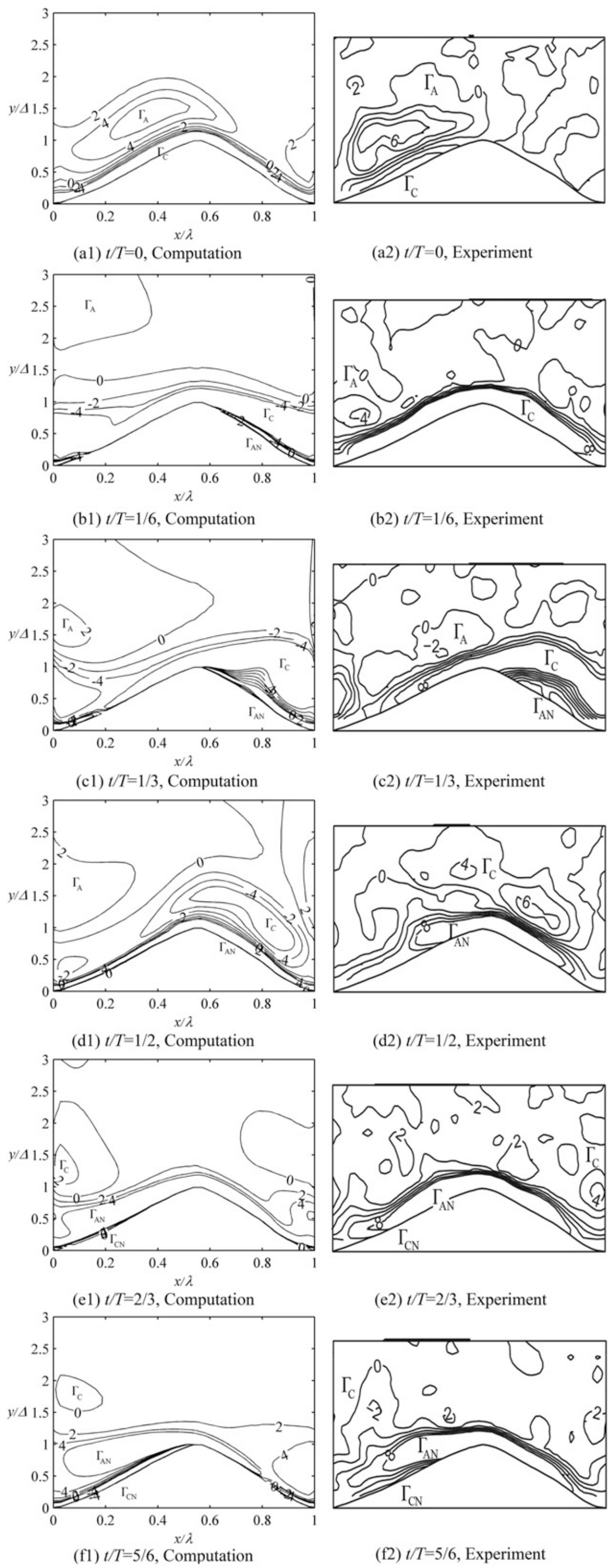

FIG. 8. Comparison of (left) computed nondimensional vorticity $\Omega\lambda/U_m$ with (right) van der Werf et al.'s (2007, 2008) experimental measurement.

direction at $t/T = 1/2$, the clockwise vortex is finally swept away while a new anticlockwise vortex starts to form at the left-hand (lee) side below the clockwise vortex (Fig. 4g), and the process repeats itself. The life cycle of vortex and its surrounding flow can be illustrated in Fig. 5.

For a quantitative description of the vortex formation–ejection process, we define the center of the vortex at a moment as the point where the magnitude of velocity $|\mathbf{u}| = \sqrt{u^2 + v^2}$ is a local minimum within the flow. This definition is simple and good enough in the present discussions, even though a more accurate method for the identification of a vortex center is also available. Considering that the center of the vortex is in principle a point where the vorticity $\omega = \partial v/\partial x - \partial u/\partial y$ is a local extremum, we may use the distance between the center of the vortex to its nearest point where the vorticity is reduced by half to represent the scale of the vortex core and denote it by R. Therefore, the strength of the vortex may be represented by the circulation around the vortex core, that is, along a circle C with its center coinciding with the center of the vortex and its radius equal to R. The strength of the vortex can thus be expressed as $\Gamma = \oint_C \mathbf{u} \cdot d\mathbf{l} = \int_A \omega\, dA$, where A is the area of C, and can be numerically evaluated by summing up the product of the discrete value of ω with the relevant area of the grid over the whole vortex core. In Fig. 6a, we plot the trajectory of the vortex center for Nakato et al.'s (1977) experimental case. The temporal variations of the dimensionless scale of the vortex $\Lambda = R/\sqrt{\lambda\Delta}$ and of the dimensionless strength of the vortex $\Psi = \Gamma/(\lambda\Delta T^{-1})$ are shown in Figs. 6b and 6c, respectively. It becomes evident that the growth of the vortex core continues even after the free streamflow entered the deceleration phase, which is accompanied by a further shift of the vortex center in the horizontal direction. This is probably an effect of the diffusion of the angular momentum stored during flow acceleration. Figure 6c together with Fig. 6a also implies that the strength of the vortex decreases rapidly during ejection.

The vortex dynamics may also be discussed by means of the swirling strength defined by Chong et al. (1990) and Zhou et al. (1999). In a two-dimensional flow, the swirling strength can be expressed by $\Phi = \sqrt{Q}$ if $Q > 0$ and $\Phi = 0$ if $Q < 0$, where $Q = (\partial u/\partial x)(\partial v/\partial y) - (\partial u/\partial y)(\partial v/\partial x)$. There are a number of studies that showed the effectiveness of using swirling strength to describe the vortices (Nichols and Foster 2007, 2009; Penko et al. 2013) in spite of its invalidity in identifying the direction of the rotation of a vortex. Figure 7 presents the contours of the nondimensional swirling strength $\Phi\lambda/U_m$ at the different phase of the oscillatory flow of Nakato et al.'s (1977) experimental case. In Fig. 7, Γ with its first subscript B or F representing backward or forward and its second subscript

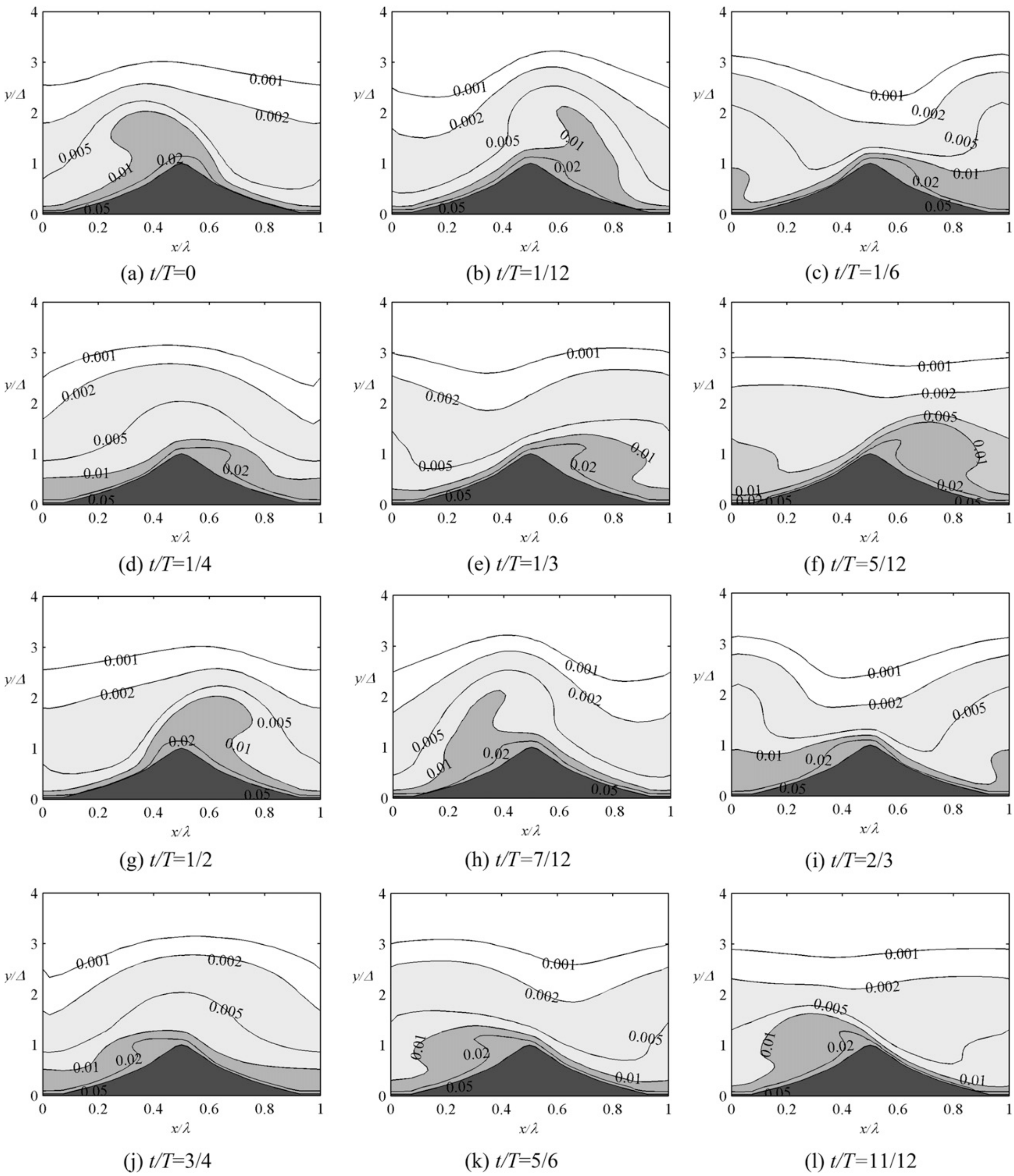

FIG. 9. Computed sediment volumetric concentration of Nakato et al.'s (1977) experimental case.

T or F representing trapped or free, denotes a vortex. It is shown that there exist two major vortex cores with very different behaviors: one is trapped by the ripple crest, and the other corresponds to the vortex that undergoes a formation–ejection process as discussed above, called the free vortex. The trapped vortex core is evidently of a large swirling strength. A similar vortex was also observed experimentally and numerically by Penko et al. (2013). In the computational results, a trapped vortex Γ_{BT} is found to be induced by the backward streamflow at $t/T = -1/12$

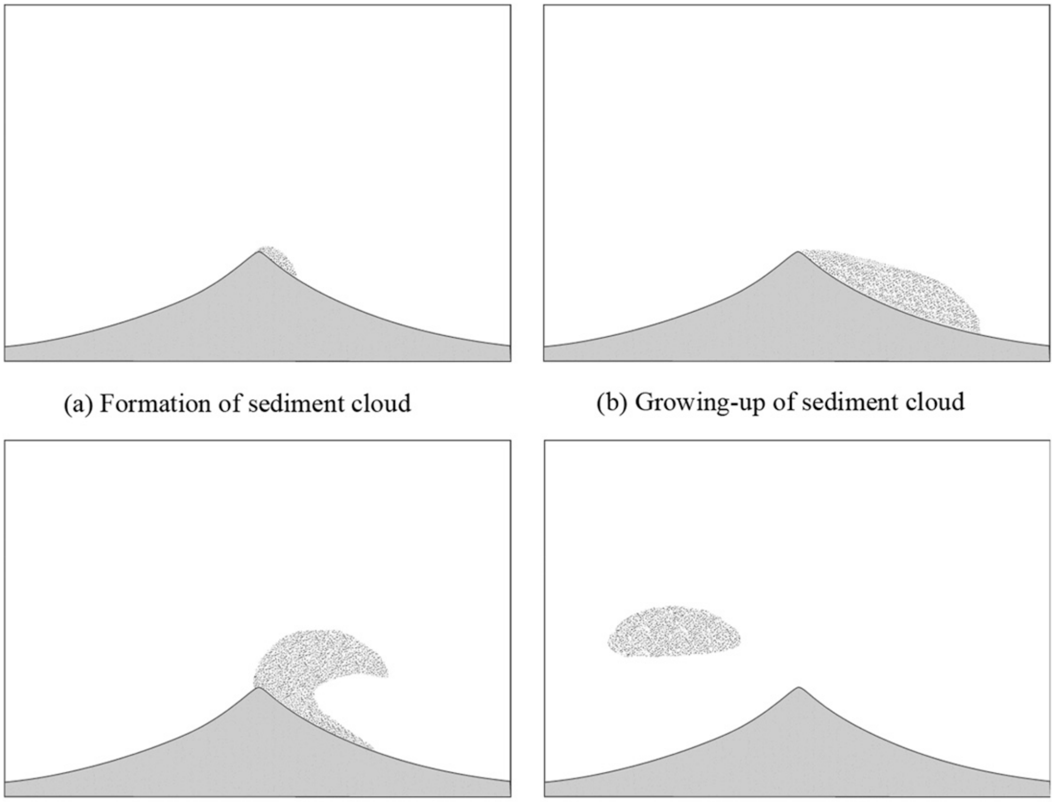

(a) Formation of sediment cloud (b) Growing-up of sediment cloud

(c) Lifting of sediment cloud (d) Backward sweeping of sediment cloud

FIG. 10. Sketch of sediment trapping–lifting process.

or, equivalently, at $t/T = 11/12$ (Fig. 7l). The swirling strength of this vortex increases until $t/T = 1/6$ and then decreases until $t/T = 5/12$ when a new trapped vortex Γ_{FT} is induced by the forward streamflow in Fig. 7f. The free vortex Γ_{FF} seems to be released from the trapped vortex induced by the backward flow during the period from $t/T = 1/12$ to $t/T = 1/4$. It becomes evident after $t/T = 1/4$, as shown in Figs. 7d–i. The swirling strength of the free vortex continues to increase until the vortex is ejected by the reversed flow in Fig. 7g. After that the swirling strength decreases significantly while a new free vortex Γ_{BF} is generated by the forward flow. The importance of the free vortex to sediment pickup, suspension, and transport now becomes evident because the vortex rises up with an increasing swirling strength and is ejected over the ripple.

For a direct comparison of the numerical results on the periodic development and decay of vortex with experiments, case Mr5b63 of van der Werf et al. (2007, 2008) is also studied. The free-stream velocity in this case is $U = U_1 \cos\sigma(t + t_0) + U_2 \cos2\sigma(t + t_0)$, where $U_1 = 0.54\,\mathrm{m\,s^{-1}}$, $U_2 = 0.09\,\mathrm{m\,s^{-1}}$, and $t_0/T = -0.224$. A comparison of the computed nondimensional vorticity $\Omega\lambda/U_m$ with the experimental results is given in Fig. 8. The agreement between the present computation and the experiment of van der Werf et al. (2007, 2008) is shown to be reasonably good. It is also seen that a clockwise vortex Γ_{C} begins to form at $t/T = 1/6$. This vortex grows up and is finally ejected and faded away at $t/T = 2/3$. At the same time, an anticlockwise vortex Γ_{A} begins to form by the reversed flow. This vortex formation–ejection process is similar as in Nakato et al.'s (1977) experimental case that we discussed based on the computed flow velocity and the computed swirling strength.

d. *Process of sediment entrainment*

Figure 9 shows the intrawave variation of the sediment volumetric concentration obtained with the present numerical model for Nakato et al.'s (1977) experimental case. The contours in the figure correspond to constant values of the volumetric concentration. Note that the layer with concentration varying from 0.05 to its maximum value of 0.6 is too thin to be distinguished. The numerical results indicate that the process of sediment motion over a ripple bed is very different from the typical situation over a flat bottom, which is simply characterized by an intensive

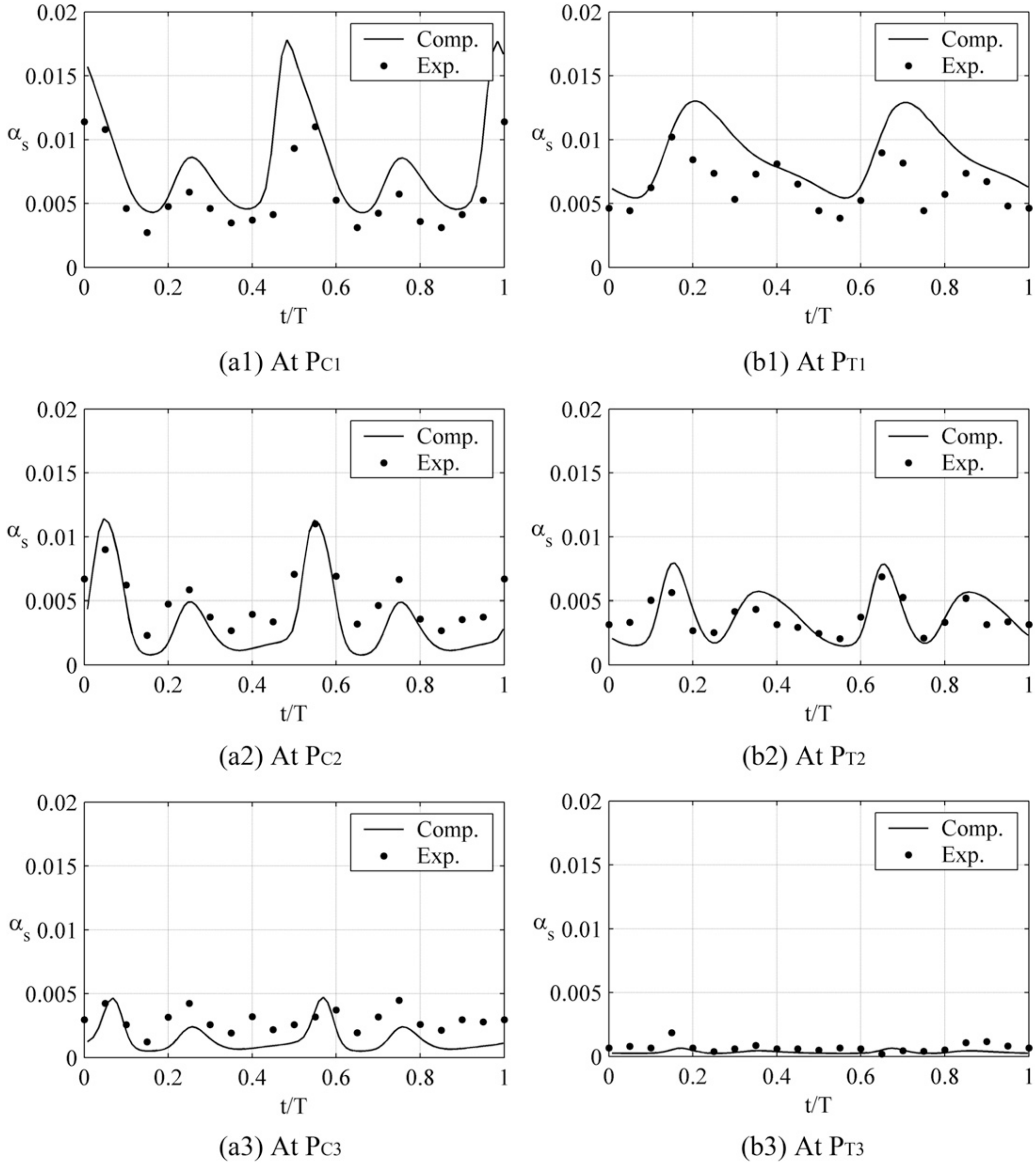

FIG. 11. Comparison of computed sediment volumetric concentration with Nakato et al.'s (1977) experimental measurement.

entrainment of sediment under the peak velocity of the oscillatory flow and an evident settling of sediment when the free-stream velocity changes its direction. Because the ripples play a dominate role, a clear process of sediment trapping and lifting can be observed in Fig. 9. Shortly after $t/T = 0$, when a vortex starts to form at the right-hand (lee) side of the ripple crest, a relatively high concentration region also appears at this position (Fig. 9b). Then, the high concentration region gradually expands as the scale and strength of the vortex increases since sediments are heavily entrained from the bed and are trapped in the vortex (Figs. 9c–f). Finally, the sediment cloud is ejected to a higher position over the crest and is swept toward the left-hand side of the ripple crest after the flow reverses (Fig. 9g). At the same time when the flow reverses, a relatively high concentration region starts to appear at the left-hand (lee) side of the ripple crest (Fig. 9i), and the process repeats itself. The sediment trapping–lifting process can also be sketched in Fig. 10. It is closely related to the vortex formation–ejection process depicted in Figs. 4, 5, 6, 7, and 8 and is thus a unique phenomenon over sandy ripples.

Figure 11 compares the computed temporal variation of the sediment volumetric concentration with the

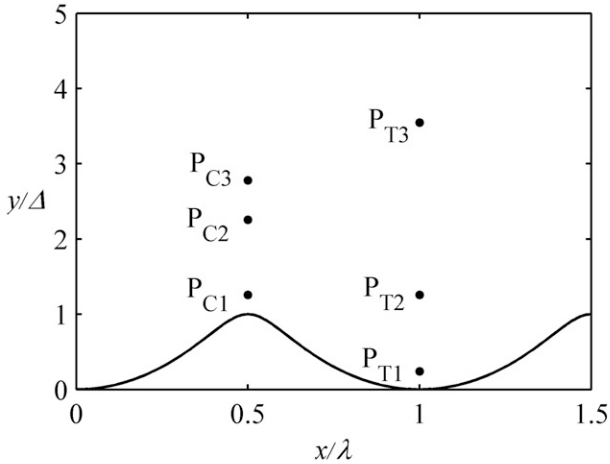

FIG. 12. Concentration measurement points in Nakato et al.'s (1977) experimental case.

measurement of Nakato et al. (1977) at six points as indicated in Fig. 12 by P_{C1}, P_{C2}, P_{C3}, P_{T1}, P_{T2}, and P_{T3}. Among these points, P_{C1}, P_{C2}, and P_{C3} are located over the ripple crest, while P_{T1}, P_{T2}, and P_{T3} are located over the ripple trough. Reasonable agreement between the computational results and experimental data is obviously obtained. As it is expected, the magnitude of volumetric concentration reduces with height in the vertical direction from P_{C1} to P_{C3} and from P_{T1} to P_{T3}. Both the computation and measurement in Fig. 11 show that the period of variation of the sediment concentration is half of the period of the free-stream oscillatory flow. This, however, is only true right over the ripple crest or trough because of the symmetry of the ripple geometry.

It is of interest to note that the temporal variation of the sediment volumetric concentration has four peaks within a period of the oscillatory flow as shown in Fig. 11. Referring to Figs. 4, 7, and 9, we understand that two of these peaks correspond to the ejection of the vortex, and the other two correspond to sweeping of the ejected vortex by the reversed flow.

For a further verification, the numerical results on the intrawave variation of the sediment volumetric concentration of van der Werf et al.'s (2007, 2008) case Mr5b63 are compared with the measurements in Fig. 13. The agreement between the present computation and van der Werf et al.'s (2007, 2008) experiment is shown to be generally good. Some phase difference may be observed between the computed and measured results at $t/T = 2/3$ for $y/\Delta > 1.5$. This difference, however, may not be a problem of the numerical model because it was also reported in van der Werf et al.'s (2008) study. It is necessary to emphasize that the intrawave variation of the sediment cloud in Fig. 13 has a very close correlation

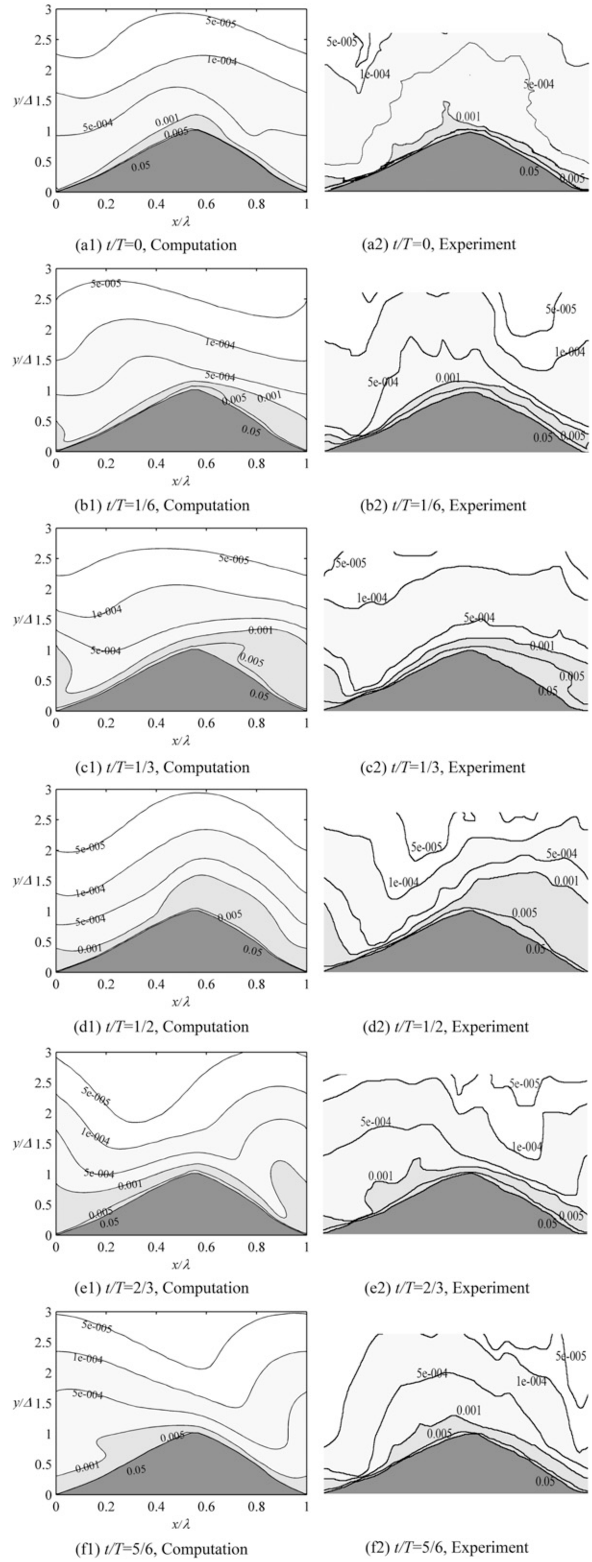

FIG. 13. Comparison of the (left) computed sediment volumetric concentration with (right) van der Werf et al.'s (2007, 2008) experimental measurement.

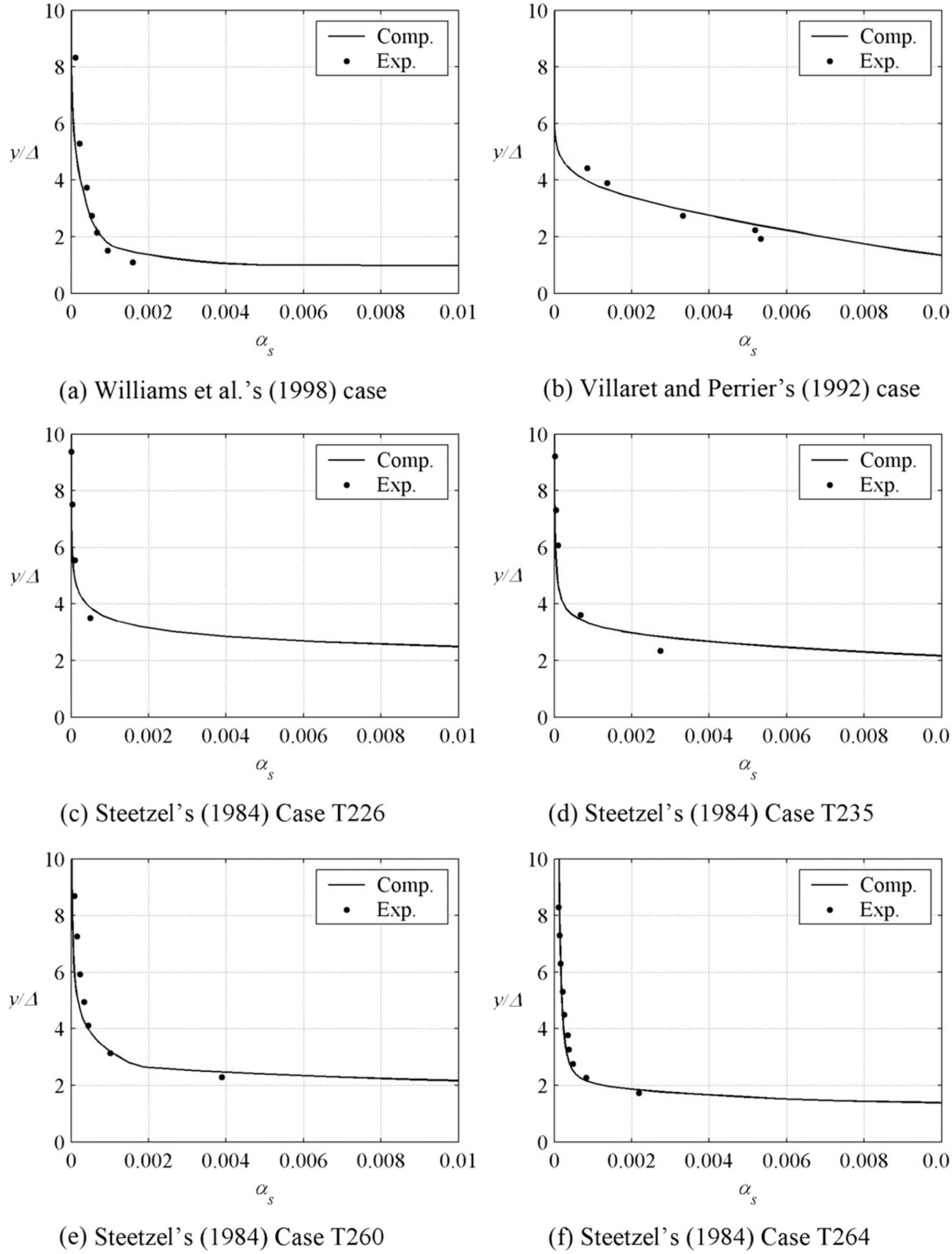

FIG. 14. Comparison of computed, mean, sediment volumetric concentration with experiments.

with the vorticity contours for the same problem as shown in Fig. 8.

e. Net sediment transport

To show the feasibility of our numerical model for the prediction of the regional topography change because of sediment motion, we pay some attention to the vertical distribution of the sediment volumetric concentration averaged over a period of the free streamflow and over a wavelength of the ripple as well. Figure 14 shows the comparison of the computed results with the experimental data of Williams et al. (1998), Villaret and Perrier (1992), and Steetzel (1984). In all cases, the overall agreement between the present computation and experiment is reasonably good. It is worthwhile to point out that the diameter of sediment particles used in these experiments varies from 0.09 to 0.27 mm, and the amplitude of the free-stream velocity varies from 0.2 to $0.75\,\mathrm{m\,s^{-1}}$. As a result, the scale of the vortex ripples covers a wide range. In addition, Steetzel's (1984) experiments include four cases, that is, cases T226, T235, T260, and T264, of which the amplitude of the free-stream velocity differs while other conditions are fixed. It may also be necessary to mention that cases T226 and T264 of Steetzel's (1984) experiments cannot be regarded as vortex ripple cases based on the criterion of Thorne et al. (2009). However, the sediment concentration is still reasonably predicted by the present model as long as the ripples are stable and the ripple profiles used in the computations are accurate enough.

4. Conclusions

This study uses a two-phase turbulent flow model to study the sediment motion over equilibrium sandy ripples with regular geometry. The numerical results show good agreement with the data of the intrawave fluid and sediment motion obtained by different investigators either in oscillatory flow tunnels or in wave flumes. For both the clear water flow over fixed solid ripples and sediment-laden flow over sandy ripples, the wavy variation of the horizontal velocity in the vertical direction, which has an equivalent scale to the ripple height and is related to the presence of the vortex that always accompanies the oscillatory flow over a ripple, has been confirmed. The dynamic process of the vortex generation, growth, ejection, and finally being swept over a sandy ripple bed can also be well represented by the numerical model. The sediment trapping–lifting process associated with the formation–ejection process of vortices has also been demonstrated. The temporal variation of the sediment volumetric concentration at a fixed point is shown to have four peaks within a period of the oscillatory flow, of which two correspond to the ejection of a highly concentrated sediment cloud and the others correspond to sweeping of the ejected sediment cloud as the flow reverses.

Acknowledgments. This research is supported by Natural Science Foundation of China (NSFC) under Grant 11472156 and by State Key Laboratory of Hydroscience and Engineering, China, under Grant 2014-KY-02.

REFERENCES

Ahilan, R. V., and J. Sleath, 1987: Sediment transport in oscillatory flow over flat beds. *J. Hydraul. Eng.,* **113,** 308–322, doi:10.1061/(ASCE)0733-9429(1987)113:3(308).

Andersen, K. H., 1999: The dynamics of ripples beneath surface wave and topics in shell models of turbulence. Ph.D. dissertation, University of Copenhagen, 284 pp.

——, and C. Faraci, 2003: The wave plus current flow over vortex ripples at an arbitrary angle. *Coastal Eng.,* **47,** 431–441, doi:10.1016/S0378-3839(02)00158-8.

Aydin, I., and N. Shuto, 1988: An application of the k-ε model to oscillatory boundary layers. *Coastal Eng. J.,* **30,** 11–24.

Ayrton, H., 1910: Origin and growth of ripple mark. *Proc. Roy. Soc. London,* **A84,** 285–310, doi:10.1098/rspa.1910.0076.

Bagnold, R. A., 1946: Motion of wave in shallow water, interaction between waves and sand bottoms. *Proc. Roy. Soc. London,* **A187,** 1–18, doi:10.1098/rspa.1946.0062.

Bakhtyar, R., A. Yeganeh-Bakhtiary, D. A. Barry, and A. Ghaheri, 2009: Two-phase hydrodynamic and sediment transport modeling of wave-generated sheet flow. *Adv. Water Resour.,* **32,** 1267–1283, doi:10.1016/j.advwatres.2009.05.002.

Blondeaux, P., and G. Vittori, 1990: Oscillatory flow and sediment motion over a ripples bed. *Proc. 22nd Int. Conf. on Coastal Engineering,* Delft, Netherlands, ASCE, 2186–2199.

——, and ——, 1991: Vorticity dynamics in an oscillatory flow over a rippled bed. *J. Fluid Mech.,* **226,** 257–289, doi:10.1017/S0022112091002380.

Camenen, B., 2009: Estimation of the wave-related ripple characteristics and induced bed shear stress. *Estuarine Coastal Shelf Sci.,* **84,** 553–564, doi:10.1016/j.ecss.2009.07.022.

Carstens, M. R., F. M. Neilson, and H. D. Altinbilek, 1969: Bed forms generated in laboratory under an oscillatory flow: Analytical and experimental study. Coastal Engineering Research Centre Tech. Memo. 28, 102 pp.

Chang, Y. S., and A. Scotti, 2003: Entrainment and suspension of sediments into a turbulent flow over ripples. *J. Turbul.,* **4,** 1–21, doi:10.1088/1468-5248/4/1/019.

Chen, X., Y. Li, X. Niu, D. Chen, and X. Yu, 2011a: A two-phase approach to wave-induced sediment transport under sheet flow conditions. *Coastal Eng.,* **58,** 1072–1088, doi:10.1016/j.coastaleng.2011.06.003.

——, ——, ——, M. Li, D. Chen, and X. Yu, 2011b: A general two-phase turbulent flow model applied to the study of sediment transport in open channels. *Int. J. Multiphase Flow,* **37,** 1099–1108, doi:10.1016/j.ijmultiphaseflow.2011.05.013.

Chong, M. S., A. E. Perry, and B. J. Cantwell, 1990: A general classification of three-dimensional flow fields. *Phys. Fluids,* **2A,** 765–777, doi:10.1063/1.857730.

Chou, Y.-J., and O. B. Fringer, 2010: A model for the simulation of coupled flow-bed form evolution in turbulent flows. *J. Geophys. Res.,* **115,** C10041, doi:10.1029/2010JC006103.

Darwin, G. H., 1883: On the formation of ripple-mark in sand. *Proc. Roy. Soc. London,* **36,** 18–43, doi:10.1098/rspl.1883.0077.

Dingier, J. R., and D. L. Inman, 1976: Wave-formed ripples in nearshore sands. *Proc. 15th Int. Conf. on Coastal Eng.,* Honolulu, HI, ASCE, 2109–2126.

Dumas, S., R. Arnott, and J. B. Southard, 2005: Experiments on oscillatory-flow and combined-flow bed forms: Implications for interpreting parts of the shallow-marine sedimentary record. *J. Sediment. Res.,* **75,** 501–513, doi:10.2110/jsr.2005.039.

Elghobashi, S., and T. W. Abou-Arab, 1983: A two-equation turbulence model for two-phase flows. *Phys. Fluids,* **26,** 931–938, doi:10.1063/1.864243.

Faraci, C., and E. Foti, 2002: Geometry, migration and evolution of small scale bedforms generated by regular and irregular waves. *Coastal Eng.,* **47,** 35–52, doi:10.1016/S0378-3839(02)00097-2.

Fredsoe, J., K. H. Andersen, and B. M. Summer, 1999: Wave plus current over a ripple-covered bed. *Coastal Eng.,* **38,** 177–221, doi:10.1016/S0378-3839(99)00047-2.

Greenwood, B., and R. A. Davis, 1984: *Hydrodynamics and Sedimentation in Wave-Dominated Coastal Environments.* Elsevier, 473 pp.

Hansen, E., J. Fredsoe, and R. Deigaard, 1994: Distribution of suspended sediment over wave-generated ripples. *J. Waterw. Port Coastal Ocean Eng.,* **120,** 37–55, doi:10.1061/(ASCE)0733-950X(1994)120:1(37).

Hinze, J. O., 1975: *Turbulence.* McGraw-Hill, 790 pp.

Hsu, T., J. T. Jenkins, and P. Liu, 2004: On two-phase sediment transport: Sheet flow of massive particles. *Proc. Roy. Soc. London,* **A460,** 2223–2250, doi:10.1098/rspa.2003.1273.

Jha, S. K., and F. A. Bombardelli, 2009: Two-phase modeling of turbulence in dilute sediment-laden, open-channel flows. *Environ. Fluid Mech.,* **9,** 237–266, doi:10.1007/s10652-008-9118-z.

Kennedy, J. F., and M. Falcon, 1965: Wave generated sediment ripples. MIT Hydrodynamics Laboratory Rep. 86, 55 pp.

Kim, H., B. A. O'Connor, T. H. Kim, and J. J. William, 2000: Suspended sediment concentration over ripples. *Proc. 27th Int. Conf. on Coastal Engineering,* Sydney, Australia, ASCE, 2873–2885.

Lewis, A. W., and Coauthors, 1995: Flow over ripples: Models and experiments. *Proc. Second Int. Conf. on Coastal Dynamics,* Gdynia, Poland, ASCE, 686–697.

Li, M., and B. A. O'Connor, 2007: Numerical study of sediment transport above rippled beds under combined waves and currents. *Sedimentology,* **54,** 1345–1363, doi:10.1111/j.1365-3091.2007.00884.x.

Lofquist, K. E. B., 1978: Sand ripple growth in an oscillatory-flow water tunnel. USACE Coastal Engineering Research Centre Tech. Paper 78-5, 100 pp.

Longo, S., 2005: Two-phase flow modeling of sediment motion in sheet-flows above plane beds. *J. Hydraul. Eng.,* **131,** 366–379, doi:10.1061/(ASCE)0733-9429(2005)131:5(366).

Longuet-Higgins, M. S., 1981: Oscillating flow over steep sand ripples. *J. Fluid Mech.,* **107,** 1–35, doi:10.1017/S0022112081001651.

Malarkey, J., and A. G. Davies, 2002: Discrete vortex modelling of oscillatory flow over ripples. *Appl. Ocean Res.,* **24,** 127–145, doi:10.1016/S0141-1187(02)00035-4.

——, and ——, 2004: An eddy viscosity formulation for oscillatory flow over vortex ripples. *J. Geophys. Res.,* **109,** C12016, doi:10.1029/2003JC002086.

Mellor, G., 2002: Oscillatory bottom boundary layers. *J. Phys. Oceanogr.,* **32,** 3075–3088, doi:10.1175/1520-0485(2002)032<3075:OBBL>2.0.CO;2.

Mogridge, G. R., and J. W. Kamphuis, 1972: Experiments on bed form generation by wave action. *Proc. 13th Int. Conf. on Coastal Engineering,* Vancouver, Canada, ASCE, 1123–1142.

Nakato, T., F. Locher, J. Glover, and J. Kennedy, 1977: Wave entrainment of sediment from rippled bed. *J. Waterw. Port Coastal Ocean Div.,* **103,** 83–99.

Nichols, C. S., and D. L. Foster, 2007: Full-scale observations of wave-induced vortex generation over a rippled bed. *J. Geophys. Res.,* **112,** C10015, doi:10.1029/2006JC003841.

——, and ——, 2009: Observations of bed form evolution with field-scale oscillatory hydrodynamic forcing. *J. Geophys. Res.,* **114,** C08010, doi:10.1029/2008JC004733.

Nielsen, P., 1992: *Coastal Bottom Boundary Layers and Sediment Transport.* World Scientific, 324 pp.

O'Donoghue, T., and G. Clubb, 2001: Sand ripples generated by regular oscillatory flow. *Coastal Eng.,* **44,** 101–115, doi:10.1016/S0378-3839(01)00025-4.

——, J. S. Doucette, J. J. van der Werf, and J. S. Ribberink, 2006: The dimensions of sand ripples in full-scale oscillatory flows. *Coastal Eng.,* **53,** 997–1012, doi:10.1016/j.coastaleng.2006.06.008.

Pedocchi, F., and M. H. García, 2009a: Ripple morphology under oscillatory flow: 1. Prediction. *J. Geophys. Res.,* **114,** C12014, doi:10.1029/2009JC005354.

——, and ——, 2009b: Ripple morphology under oscillatory flow: 2. Experiments. *J. Geophys. Res.,* **114,** C12015, doi:10.1029/2009JC005356.

Penko, A. M., J. Calantoni, S. Rodriguez-Abudo, D. L. Foster, and D. N. Slinn, 2013: Three-dimensional mixture simulations of flow over dynamic rippled beds. *J. Geophys. Res. Oceans,* **118,** 1543–1555, doi:10.1002/jgrc.20120.

Ranasoma, K., and J. F. A. Sleath, 1992. Velocity measurements close to rippled beds. *Proc. 23th Int. Conf. on Coastal Engineering,* Venice, Italy, ASCE, 2383–2396.

Ribberink, J. S., and A. A. Al-Salem, 1994: Sediment transport in oscillatory boundary layers in cases of rippled beds and sheet flow. *J. Geophys. Res.,* **99,** 12 707–12 727, doi:10.1029/94JC00380.

Rousseaux, G., 2006: Physical distinction between rolling-grain ripples and vortex ripples: An experimental study. *Phys. Rev. E Stat. Nonlinear Soft Matter Phys.,* **74,** 066305, doi:10.1103/PhysRevE.74.066305.

Sato, S., and K. Horikawa, 1986: Laboratory study on sand transport over ripples due to asymmetric oscillatory flows. *Proc. 20th Int. Conf. on Coastal Engineering,* Taipei, Taiwan, ASCE, 1481–1495.

——, N. Mimura, and A. Watanabe, 1984: Oscillatory boundary layer flow over rippled beds. *Proc. 19th Int. Conf. on Coastal Engineering,* Houston, TX, ASCE, 2293–2309.

——, H. Uehara, and A. Watanabe, 1986: Numerical simulation of the oscillatory boundary layer flow over ripples by a k-ε turbulence model. *Coastal Eng. J.,* **29,** 65–78.

Schiller, L., and A. Naumann, 1935: A drag coefficient correlation. *Z. Ver. Deutsch. Ing.,* **77,** 318–320.

Sleath, J. F. A., 1982: Friction coefficients of rippled beds in oscillatory flow. *Cont. Shelf Res.,* **1,** 33–47, doi:10.1016/0278-4343(82)90031-0.

——, 1984: *Sea Bed Mechanics.* Wiley, 335 pp.

——, 2000: Ripple geometry under serve wave condition. *Proc. 27th Int. Conf. on Coastal Engineering,* Sydney, Australia, ASCE, 2686–2699.

Steetzel, H. J., 1984: Sediment suspension under oscillatory wave conditions just above the sand bed. MSc. Thesis, Coastal Engineering Department, Delft University of Technology, 216 pp.

Tam, C. K. W., 1969: The drag on a cloud of spherical particles in low Reynolds number flow. *J. Fluid Mech.,* **38,** 537–546, doi:10.1017/S0022112069000322.

Thorne, P. D., J. J. Williams, and A. G. Davies, 2002: Suspended sediments under waves measured in a large-scale flume facility. *J. Geophys. Res.,* **107,** doi:10.1029/2001JC000988.

——, A. G. Davies, and P. S. Bell, 2009: Observations and analysis of sediment diffusivity profiles over sandy rippled beds under waves. *J. Geophys. Res.,* **114,** C02023, doi:10.1029/2008JC004944.

Tsujimoto, G., N. Hayakawa, M. Ichiyama, Y. Fukushima, and Y. Nakamura, 1991: A study on suspended sediment concentration and sediment transport mechanism over rippled sand bed using a turbulence model. *Coastal Eng. J.,* **34,** 177–189.

van der Werf, J. J., J. S. Doucette, T. O'Donoghue, and J. S. Ribberink, 2007: Detailed measurements of velocities and suspended sand concentrations over full-scale ripples in regular oscillatory flow. *J. Geophys. Res.,* **112,** F02012, doi:10.1029/2006JF000614.

——, V. Magar, J. Malarkey, K. Guizien, and T. O'Donoghue, 2008: 2DV modelling of sediment transport processes over full-scale ripples in regular asymmetric oscillatory flow. *Cont. Shelf Res.,* **28,** 1040–1056, doi:10.1016/j.csr.2008.02.007.

Villaret, C., and G. Perrier, 1992: Transport of fine sand by combined waves and current: An experimental study. Direction Des Etudes et Recherches, Électricite de France Rep. E4202R, 81 pp.

Williams, J. J., P. S. Bell, L. E. Coates, P. J. Hardcastle, J. D. Humphery, S. P. Moores, P. D. Thorne, and K. Trouw, 1998: Evaluation of field equipment used studies of sediment dynamics. Proudman Oceanographic Laboratory Rep. 53, 45 pp.

——, ——, P. D. Thorne, N. Metje, and L. E. Coates, 2004: Measurement and prediction of wave-generated suborbital ripples. *J. Geophys. Res.,* **109,** C02004, doi:10.1029/2003JC001882.

Zedler, E. A., and R. L. Street, 2006: Sediment transport over ripples in oscillatory flow. *J. Hydraul. Eng.,* **132,** 180–193, doi:10.1061/(ASCE)0733-9429(2006)132:2(180).

Zhou, J., R. J. Adrian, S. Balachandar, and T. M. Kendall, 1999: Mechanisms for generating coherent packets of hairpin vortices in channel flow. *J. Fluid Mech.,* **387,** 353–396, doi:10.1017/S002211209900467X.